# TUDelft

Delft University of Technology

## Multi-Level Characterization of Lignite MineWaste by the Integration of Wide Wavelength Range Infrared Spectroscopy

Kamps, Oscar; Desta, Feven; Maghsoudi Moud, Fardad; Buxton, Mike

**Important note**
To cite this publication, please use the final published version (if applicable).
Please check the document version above.

# Multi-Level Characterization of Lignite Mine Waste by the Integration of Wide Wavelength Range Infrared Spectroscopy

Oscar Kamps *, Feven Desta *, Fardad Maghsoudi Moud and Mike Buxton

Geoscience and Engineering Department, Delft University of Technology, Stevinweg 1, 2628 CN Delft, The Netherlands; f.maghsoudimoud@tudelft.nl (F.M.M.); m.w.n.buxton@tudelft.nl (M.B.)
* Correspondence: o.m.kamps@tudelft.nl (O.K.); f.s.desta@tudelft.nl (F.D.)

**Abstract:** Both the mineralogy and geochemistry of coal mine waste presents environmental and social challenges while simultaneously offering the potential source for recovery of metals, including critical raw materials (CRMs). Assessing these challenges and opportunities requires effective waste management strategies and comprehensive material characterization. This study deals with the integration of analytical data obtained from various portable sensor technologies. Infrared reflection spectroscopy (covering a wide wavelength range of 0.4 to 15 μm), and geochemical x-ray fluorescence (XRF) were utilized to differentiate between samples belonging to various geological lithologies and quantify elements of interest. Therefore, we developed a methodological framework that encompasses data integration and machine learning techniques. The model developed using the infrared data predicts the Sr concentration with a model accuracy of $R^2 = 0.77$ for the testing dataset; however, the model performances decreased for predicting other elements such as Pb, Zn, Y, and Th. Despite these limitations, the approach demonstrates better performance in discriminating materials based on both mineralogical and geochemical compositions. Overall, the developed methodology, enables rapid and in-situ determination of coal mine waste composition, providing insights into waste composition that are directly linked to potential environmental impact, and the possible recovery of economically valuable metals.

**Keywords:** mine waste; sensor technology; material characterization; infrared spectroscopy; geochemical analysis

## 1. Introduction

The long-term exploitation of coal in East Germany resulted in mine waste dumps with associated geotechnical and geochemical safety risks. The mineralogy or geochemistry of the coal- or sedimentary layers within the mines could be of environmental concern due to soil and water contamination, such as acid mine drainage or heavy metal leaching into the groundwater [1–3]. However, besides the environmental concerns, the waste could provide an opportunity for secondary mining for metals of economic interest [4].

The heterogeneous nature of waste dumps complicates the geochemical and mineralogical characterization [1]. Due to the processing and mixing after the extraction, the material lacks geological context and spatial coherence, which complicates spatial or volumetric analysis. Also, external conditions could cause alteration or leaching resulting in local compositional differences within the waste dump.

Because of these challenges of mine waste, the characterization or monitoring of mine waste requires innovative methods of sampling, measuring and analyzing. The challenge of sampling is to obtain representative samples from a heterogeneous waste dump. For the measurements, there are many options of various sensor technologies that can be used on various platforms such as satellites, drones and airplanes [5,6], and on the ground for sorting applications [7]. Each system and platform has its advantages and disadvantages regarding, measurement accuracy, processing time, and spatial coverage.

The present study argues that comprehensive monitoring and analysis of mine waste requires multiple sensors in combination with data integration. Therefore, we will use multiple handheld sensors such as a portable X-ray fluorescence (pXRF) device to measure the geochemistry, and two handheld infrared spectrometers to analyze the mineralogy. The results will be validated through laboratory measurements using Inductively Coupled Plasma (ICP) and X-ray diffraction (XRD). Previous studies used these sensors individually for mine waste analysis, but not as an integrated system.

It is aimed to investigate the usability of wide wavelength range infrared spectroscopy, from visible to longwave infrared wavelengths, and geochemical analysis coupled with data analysis to characterize the lignite coal mine waste in East Germany. Here, we only consider the environmental impact associated with the mineralogical and geochemical composition of mine waste. Other environmental concerns associated with lignite mine waste, such as methane emissions, which are typically related to gas within the coals, are outside the detection capabilities of our sensors. The first objective is to study the capabilities of each sensor for describing the mine waste. The second objective is to assess whether the infrared reflection data can be used for the semi-quantification of target elements in coal mine waste. With this novel combination of the use of sensor technologies and integration, we provide new insights into how mineralogy and geochemistry are linked in this specific mining area. These results are discussed regarding what sensor technologies can best be used for mine waste monitoring or analysis to study its environmental impact or potential for secondary recovery.

## 2. Geological and Analytical Background Information

### 2.1. Geological Setting

The lignite mines studied for this study are between the river Saale in the west and river Elbe in the east, just south of Leipzig, Saxony, Central Germany. The locations of the study sites are presented in Figure 1. In total, there are two open pit mines, Schleenhain and Profen, both exploited by Tagebau Vereinigtes Schleenhain. The annual production of these open mine pit sites is annually 8.5 million tons of raw lignite and an overburden of 30–38 million cubic meters per year [8]. Figure 1 outlines the current open pit in brown and the reclamation areas in dark green.

The geological history of this area is best described in the overview papers by Eissmann [9,10] on, respectively, the Quaternary and Tertiary geology. The geology of both mines is characterized by a pre-Tertiary basin, covered by Tertiary fluviatile and estuarine deposits, including the lignite deposits, and a Quaternary sedimentary overburden [9–11].

The coal layers are formed in the Cenozoic, in a fluviatile environment [10]. A transgressive epicontinental sea is the cause of a complex sedimentary system in which the coal layers are found as lenses interlayered between the other sedimentary rocks with varying seam thicknesses of tens of meters [10,11]. The sedimentary rocks vary from clays to coarse sands [10]. The overburden is Quaternary and consists of sedimentary sand, clay and silt layers [9].

The coal in the area is classified as lignite, which has 25–35% carbon and is the lowest rank coal [12]. Besides the organic matter, the coal can be associated with syngenetic minerals such as pyrite, formed by chemical processes in accumulated organic matter, and detrital minerals such as clay and silicate minerals that are deposited in the same swamp environment [12]. Among these minerals, pyrite is a considerable environmental concern, since its oxidation promotes acid mine drainage and therefore requires special reclamation actions [13–15].

Both the coal and overburden material could have a geochemical composition with environmental implication [16,17]. The overburden fluviatile sediments have source in the polymetallic area in the southeast, bordering the Czech Republic [18,19]. A study on sediments and soils in nearby sedimentary basins indicates geogenic enrichment of metals such as Cd, Co, Cu, V, Cr, Pb, Hg, Ni and Zn [16]. Various other trace elements can be associated with coal in either organic, or inorganic sulfide and non-sulfide fractions [20].
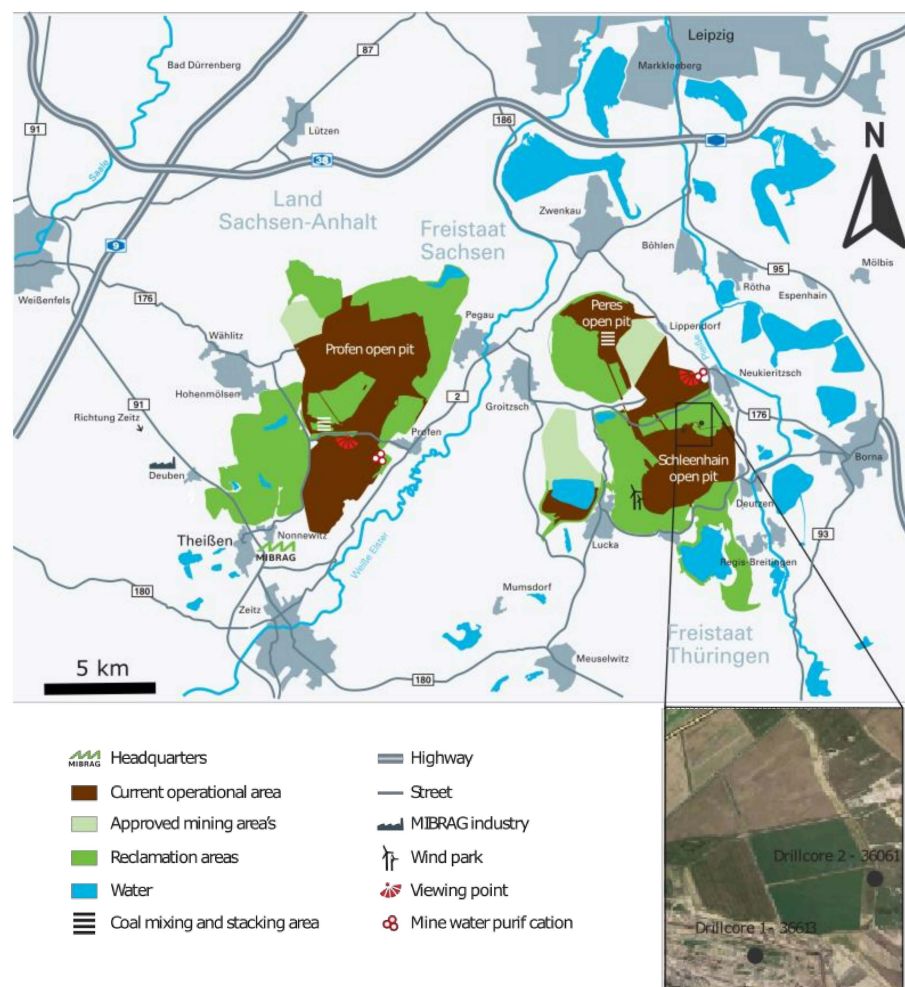
**Figure 1.** Overview map of open pit mines, MIBRAG. Edited from MIBRAG (2020). Zoom box shows the location of drill cores presented on the Google Earth base map (Google earth V 7.3.6.9796.) (22 February 2024). Breunsdorf, Germany. 51°08′16.48″ N, 12°23′47.37″ E, Eye altitude 142 m. Landsat/Copernicus. https://earth.google.com/web/@0,-3.4221001,0a,22251752.77375655d,35y, 0h,0t,0r/data=OgMKATA?authuser=0 [8 September 2021].

### 2.2. Infrared Spectroscopy

Infrared spectroscopy is the term used for the technique of analyzing spectral features in the infrared wavelength range that can be associated with material properties, such as mineral composition. This technique is becoming more conventional in mining and environmental studies due to the diverse range of measuring platforms, such as satellites, aircrafts, and handheld devices. In mining, these sensors are commonly used for example for ore and waste sorting, exploration geology and mine process monitoring [21–24].

In the literature, the infrared region of the electromagnetic spectrum is subdivided into different wavelength ranges [25]. In this work, wavelength ranges were defined as follows: visible near–infrared—VNIR (0.5–1 μm), shortwave–infrared—SWIR (1.3–2.5 μm), midwave–infrared—MWIR (2.6–5.5 μm), and longwave–infrared—LWIR (5.5–15 μm). In these wavelength ranges, different minerals produce diagnostic spectral features that can be used to identify the minerals. For example, the VNIR regions can be used for the identification of iron oxides and the SWIR for clays and carbonates [26]. The way that light scatters on a material surface varies with wavelength. Specifically, shorter wavelengths such as those in the SWIR and MWIR wavelength ranges are characterized by volume scattering, while longer wavelengths such as LWIR are dominated by surface scattering. This variation in scattering results in different spectral features across the measured wavelength range. In

case of volume scattering, the spectra are characterized by absorption features. When the sample surface scattered the light, spectral features are exhibited that can be interpreted for mineralogy. Additionally, grain size influences the scattering type. As a consequence, the same mineral could contain spectral variations in spectral characteristics [25].

The diagnostic spectral features in the VNIR wavelength range are caused by electronic absorption features of transition metals and rare earth elements [27]. The sSWIR contains mainly features associated with water and hydroxyl but also carbonates. Most spectral features are within the wavelength range from 2 to 2.5 μm, causing overlapping features that complicate the mineral identification [28]. Spectral shifts can occur due to the cation that is bonded to the OH group, and thereby the mineral chemistry can be interpreted from the spectral features [29]. The MWIR range defines the transition from volumetric- to surface-dominated scattering [25]. Both the MWIR and LWIR contain a diverse range of infrared functional groups such as borate, carbonate, sulfate, phosphate, and hydroxyl bonds [25,26]. The LWIR region is dominated by specular reflectance and therefore more sensitive to grain size [25].

Similarly to inorganic compounds like minerals, specific organic molecular bonds, such as those present in lignite coal, show unique spectral absorption features within the specified wavelength ranges. For example, the ammonia and carbon–hydrogen bonds have specific spectral absorption features in the SWIR, MWIR and LWIR wavelength regions [30–33].

## 3. Methods

### 3.1. Location and Sampling

Three sampling campaigns were conducted to collect samples from the mine pits: namely, Peres, Schleenhain, and Profen. The locations of these mine pits are presented in Figure 1 as brown polygons for current operational areas and in dark green reclamation areas. Impression of the locations of where samples are taken in the different sampling campaigns is shown in Figure 2. Unfortunately, we did not have access to samples from other lignite mines for comparison.
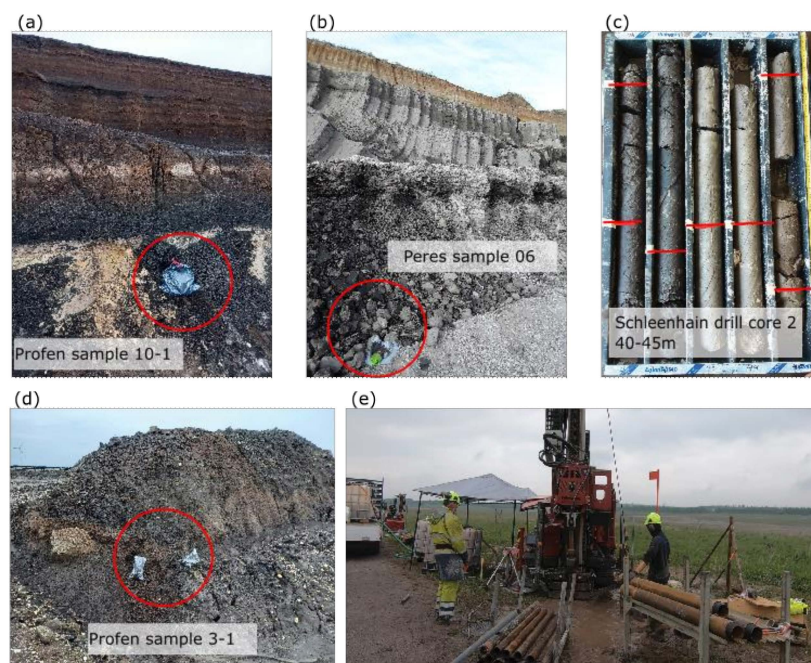


**Figure 2.** Images from the various sampling campaigns. (**a**) Samples of the Profen dataset, lithology-specific; (**b**) samples of the Schleenhain-lithology dataset; (**c**) drill core of the Schleenhain-waste; (**d**) samples of the Profen dataset, local dump site; and (**e**) drill campaign for Schleenhain-waste.

In the first sampling campaigns, samples were collected from distinctive lithologies from both the Peres and Schleenhain open pits. In this study, the dataset obtained from the first sampling campaign is named Schleenhain-lithology. The dataset consists of 30 samples in total of which 12 samples were gathered from Schleenhain, representing Tertiary sands, clays and coal seams. Likewise, in the Peres mine, 18 samples were collected from lithologies similar to those in Schleenhain, along with Quaternary gravel, clays, moraine, meltwater sand, loess, loam, and dump material.

In the second field campaign, two drill cores each with 50 m depth were used to sample the mine waste from both Schleenhain and Peres open pits. The locations are indicated within the zoom box in Figure 1, with a Google Earth map as the base. Drill core 1 is located in an area with relatively fresh mine waste, dumped a year before the drilling campaign (which is on 9 May 2022). Unlike drill core 1, the waste of the second drill core is older and deposited approximately 8 years prior to the sampling campaign. This is evident from the vegetation density in the Google Earth satellite image. Using these drill core samples, a total of 107 measurements were obtained. The measurements were taken approximately every 1 m, depending on the material variability—visually observed based on color and texture—within the drill cores. The data collected from these sample sets are referred to as Schleenhain-waste.

In the third field campaign, 28 samples were collected from the Profen area, which is found east of the Schleenhain open pit. These samples consist of a mix of lithology-specific samples and material from mine waste dump sites. The Profen dataset is utilized to assess the consistency between the lithology and mine waste samples from both Schleenhain and Profen mine pits. Although these open mine pit sites contain similar lithologies, spatial variation may lead to differences in geochemistry or mineralogy.

### 3.2. Instrumentation

Multiple handheld portable sensors, namely the Analytical Spectral Device (ASD) Fieldspec4, and Agilent Fourier Transform Infrared (FTIR) spectrometers and Niton XL5 portable X-ray fluorescence were used to acquire data using the collected samples. The instruments are shown in Figure 3. The technologies are described in the subsequent subsections. Figure 4 shows the general workflow including the sample type and the instrument used. FTIR and pXRF measurements are taken from all samples from the different sample locations. The ASD sensor was only available to be used for the Schleenhain-lithology datasets.



(a) ASD FieldSpec4  (b) FTIR Agilent 4300  (c) XRF Niton XL5

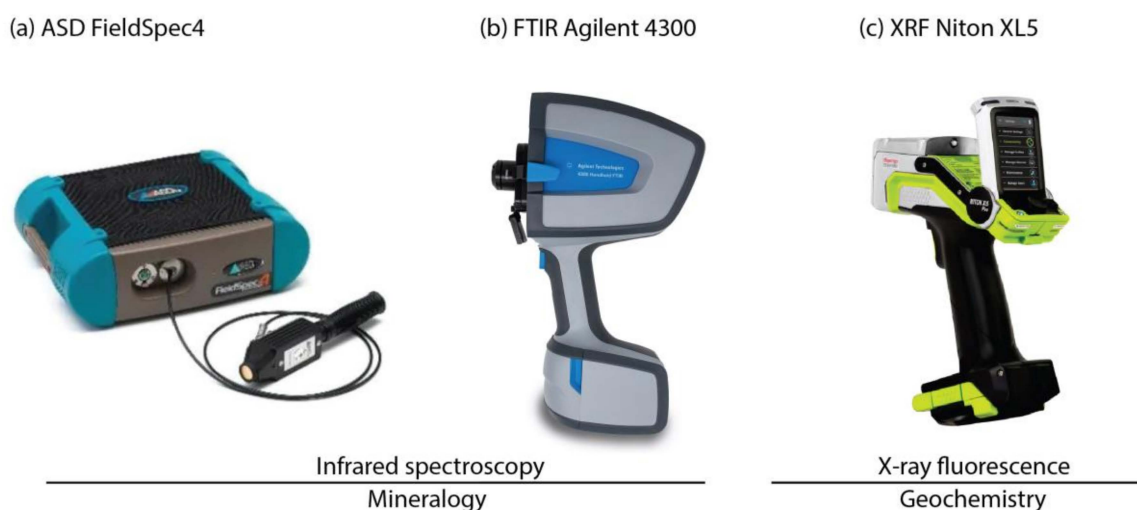Infrared spectroscopy — Mineralogy  X-ray fluorescence — Geochemistry

**Figure 3.** Portable sensors used in this study. Infrared spectrometers to analyze the mineralogy, (**a**) ASD FieldSpec4 and (**b**) Agilent FTIR. pXRF for the geochemistry, (**c**) Niton XL5.
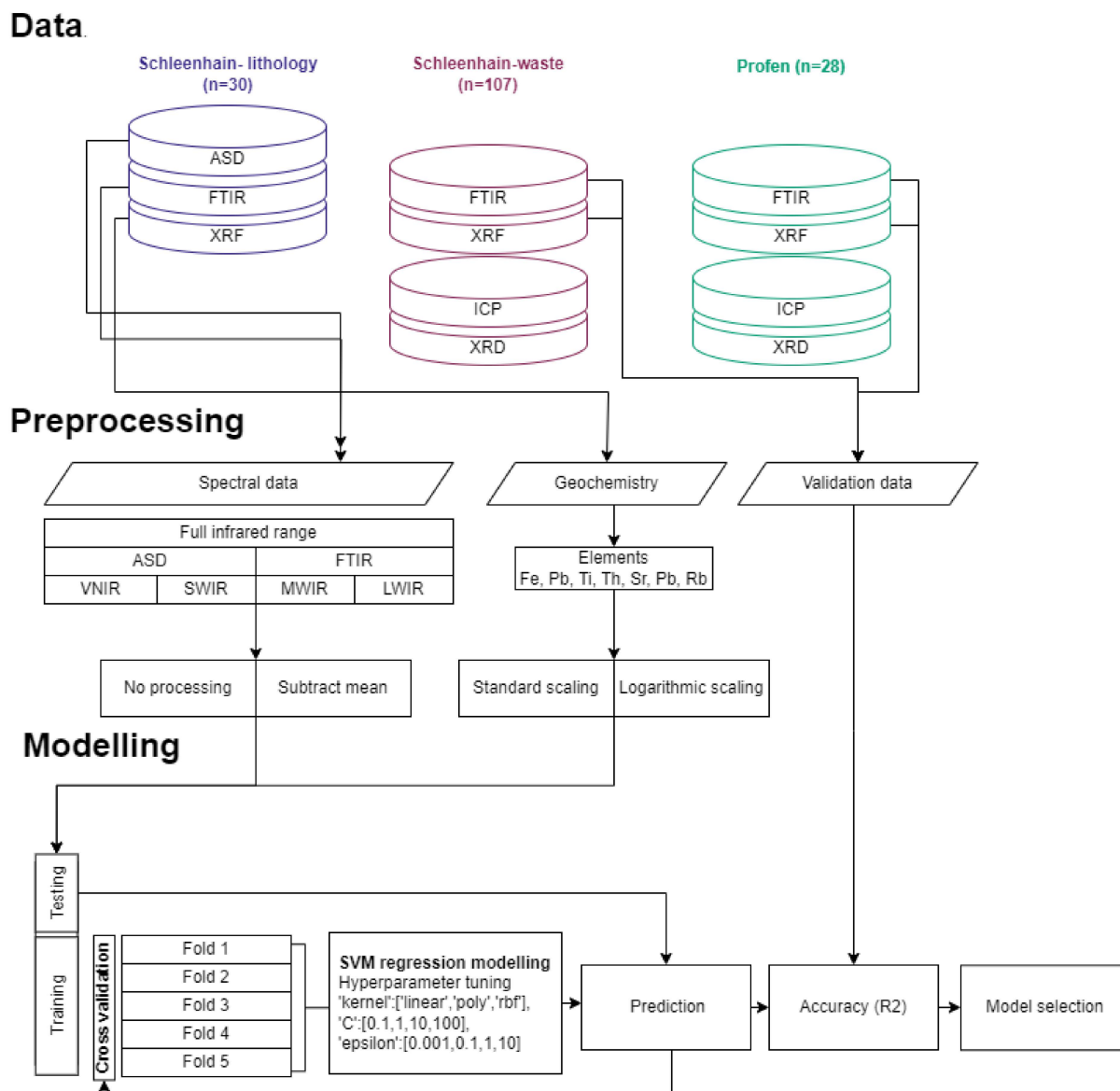
## Data



**Figure 4.** The suggested workflow for regression modelling.

3.2.1. Wide Range Infrared Spectroscopy Techniques

In this study, two infrared spectrometers, that operate over a combined spectral wavelength from 0.35 to 15.4 μm, were used to acquire infrared spectral data using the collected samples. In this study, the light frequency will be presented in wavelengths, rather than wavenumber, to stay consistent and ensure a good comparison between the spectra obtained with the ASD and FTIR.

The ASD FieldSpec4 from Malvern Panalytical is used to measure the visible and shortwave–infrared wavelength ranges from 0.35 to 2.5 μm with a spectral resolution of 3 and 8 nm in the VNIR and SWIR, respectively. When exporting the data, the spectrum is resampled to a resolution of 1 nm. The picture of the instrument is presented in Figure 3. The system is used in combination with a contact probe with a 10 mm spot size, which integrates both the optical cable and light source. The white reference calibration is carried out using a spectralon tablet. After each sample measurement, the white reference was checked and when it deviated, the sensor was recalibrated. Each measurement takes ten spectra that are later averaged in the processing of the data.

The FTIR handheld spectrometer was used to record the MWIR and LWIR data. The instrument is presented in Figure 3. The measurements were performed using the

diffuse reflectance sample interface, covering a wavelength range of 650 and 5000 cm$^{-1}$ (2.5–15.4 μm) with a 4 cm spectral resolution and a spot size of ~2 mm diameter. The standard coarse-grained silver tablet is used for calibration and reference material. We have set the measurement settings such that every 15 min, a new calibration measurement needs to be taken.

Both the ASD and FTIR sensors are portable, allowing us to measure samples directly. Given the inhomogeneity of the samples, we conducted multiple measurements to capture the compositional variance as accurately as possible. We performed approximately 3–5 measurements at different locations for each sensor, selecting sites based on our visual assessment of the compositional variability. We tried to match the measurement positions of the samples with both sensors.

### 3.2.2. X-ray Fluorescence

Geochemical data was obtained from the collected samples, at the same locations as the ASD and FTIR measurements, using the Niton XL5 Plus Handheld XRF analyzer from Thermo Scientific. The sensor has a 5 W Ag anode X-ray tube and an 8 mm spot size. The X-ray beam excites electrons from the shell of an atom. The filling of the vacant electron spot causes the release of fluorescent X-rays with an energy that can be used for geochemical quantification. The fluorescent X-ray of lighter elements is too low to either reach the detector or be recognizable compared to the background noise of the detector [34]. Therefore, the detection limit is different per element and higher for lighter elements.

Before the XRF data are analyzed, the element concentrations are compared to those of the ICP-MS validation dataset. The measured concentrations including the standard error of XRF data are plotted together. Only the elements with a coherent linear positive correlation between XRF and ICP are used for further analysis. For these elements it is concluded that the XRF measurements represent the actual sample composition.

### 3.2.3. Inductively Coupled Plasma Analysis

The conventional geochemical technique, inductively coupled plasma mass spectrometry (ICP-MS), was used to obtain the data that were employed in the validation of elemental prediction. ICP-MS is a well-established laboratory technique for elemental analysis, that can detect a wide array of elements from the periodic table at parts per million (ppm) levels. The analysis was carried out at the laboratory facility of the Utrecht University. Since ICP-MS is a lab-based analysis technique, we needed to subsample our samples. We aimed to obtain a representative sample, but given the inhomogeneous nature of the samples, achieving this was challenging. ICP-MS validation was only available for the Schleenhain-waste and Profen datasets.

### 3.2.4. X-ray Diffraction

The mineralogical composition of 28 samples (10 Profen, 18 Schleenhain-waste) were analyzed using the X-ray diffraction (XRD) technique. The measurements were performed at the Faculty ITC at the University of Twente using a Bruker D2 Phaser. The mineral interpretation is performed semi-quantitively using the DIFFRAC.EVA software version 6 and the corresponding spectral library. XRD, in combination with the Rietveld method, is the most reliable and frequently used method for mineral identification [35]. Similar to ICP-MS, XRD is a lab-based technique that also requires subsampling for analysis.

### 3.3. Exploratory Analysis
### 3.3.1. Principal Component Analysis (PCA)

Principal Component Analysis (PCA) is an exploratory analysis technique for data dimension reduction in a multivariable dataset. The algorithm defines new axes in the dataset, where the first axis explains the most variance in the data. The projection of the data points on these new axes are named score values. The contribution of the variable, in our case the individual wavelengths, are referred to as the loading values [36].

### 3.3.2. Correlation Matrix

In a correlation matrix, the covariance between variables defined by the Pearsons correlation coefficient is analyzed [37]. In this study, it is used to assess the relation between the various geochemical elemental concentrations within the three datasets and to test for correlation between the XRF and ICP-MS datasets.

### 3.4. Geochemical Modelling

The spectral measurements of a broad wavelength range coming from both infrared sensors are used to predict elemental concentrations measured with the pXRF. The general workflow of the methodological approach developed in this study is presented in Figure 4. The support vector machine regression (SVR) models were developed using the Schleenhain-lithology dataset as the training dataset and tested for Schleenhain-waste and Profen. For the Schleenhain-waste and Profen datasets, no VNIR and SWIR data are available, so only models including the FTIR wavelength range were tested on the other datasets. The blue, red and green colors indicate the colors used for the plots in the results.

### 3.4.1. Data Preparation

The geochemical modelling is done iteratively with changing pre-processing steps and testing for different wavelength ranges. The spectral data of the ASD and FTIR were combined and considered as the fused infrared wavelength range. Different models were developed to compare model performances when they were applied to the fused infrared range and individual VNIR, SWIR, MWIR and LWIR wavelength ranges. The corresponding wavelengths are defined in Background Information—Infrared Spectroscopy Section 2.2.

The pre-processing of the spectra involves averaging the measurements obtained for the same sample. For both ASD, FTIR, and pXRF, this includes the 3–5 measurements per sample. Additionally, for ASD, 10 repetitions per measurement are also averaged. For FTIR data specifically, the wavelength range between 4.15 and 4.5 μm is masked, as this range sometimes contains spectral peaks that are considered artifacts rather than mineralogical features.

For the geochemical modelling, the model performances were compared between spectra without additional spectral pre-processing and mean-centered spectra. Mean centering is a processing technique that subtracts the mean reflectance of the spectra from the spectral reflectance values.

The models are trained on the geochemical information of the XRF sensor for the seven elements: Fe (iron), Pb (lead), Th (thorium), Ti (titanium), Sr (strontium), Rb (rubidium), Y (yttrium) and Zn (zinc). In Results Section 5.1, the selection of these elements is explained. For each element, a separate model was developed, and model performances were compared by applying standard scaling, or logarithmic scaling data pre-processing techniques. Standard scaling means that the average element concentration is subtracted and divided by its standard deviation. For logarithmic scaling, we have calculated the base ten logarithm of the element concentration. This is a commonly used technique to deal with a skewed dataset. No data values are in the pXRF data, because these are the instrument detection limit and are not considered in the model.

### 3.4.2. Regression Modelling

The prediction models were developed using SVR. Other methods such as partial least squares regression and random forest regression were tested in earlier stages of this research; however, the models yielded lower performance and they were excluded from further analysis.

To evaluate the model performances, the Schleenhain-lithology dataset was first split into a training and testing dataset. A total of 33% of the data were allocated to the testing group, utilizing a group-based shuffle split methodology to ensure that measurements from the same sample did not appear in both the training and testing groups. Cross validation is

used when developing the models. The training dataset is split into 5 random groups, again making sure that samples from the same group end up in different cross validation groups.

The coefficient of determination ($R^2$) is used as a score value to assess the model performances. A minor difference in the formula is that in the Total Sum of Squares (TSS), we subtract the mean of the training dataset, and not the mean of the dataset. This was chosen because it better represents the goodness of fit of the data in the general prediction.

For the modelling we have used hyperparameter tuning to find the optimal parameters for the SVR model. The parameters that can be tuned for SVR are its kernel, regulation parameter (C) and the epsilon-tube (epsilon). The corresponding hyperparameter values can be found in the flowchart of Figure 4.

## 4. Results

### 4.1. Geochemical Analysis

Before we tested the integration of infrared and geochemical data, we performed some exploratory analyses of the geochemical dataset. First, the ICP measurements are used as a validation dataset to test whether the XRF measurements represent the actual sample geochemistry. These ICP measurements are only taken on a selection of samples from the Schleenhain-waste (23 out of 107 samples) and Profen datasets (13 out of 28 samples). Selection of these samples was based on initial geochemical analysis of sample variability based on the XRF data. The results are presented in Figure 5 indicating the $R^2$ values between XRF and ICP-MS measured concentrations. Based on this plot, we have chosen to focus this study on the elements, Sr, Pb, Fe, Rb, Ti, Zn, Y and Th, for further analysis and modelling. For the other elements it was concluded that because of the negative $R^2$, the XRF measurements might not present the actual element concentration. For the elements with a positive $R^2$, the data are visualized as a scatter plot with XRF data on the *x*-axis and ICP data on the *y*-axis. The error bars present the 1.5 standard deviation given as the output of the XRF measurements.

Element concentrations for the considered elements are shown in Figure 6 for all the datasets: Profen, two drill cores of Schleenhain-waste and the Schleenhain-lithology. Samples with values below the detection limit are considered as not a value and are therefore not plotted in the figure. The elements Pb and Zn are discussed in Tóth et al. [38] regarding their environmental impact. However, the measured concentrations do not exceed the 60 and 200 ppm threshold values for Pb and Zn, respectively. The n-number under the sample group name indicates the number of measurements in the plot. The other samples had values below the threshold values of the XRF and could therefore not be measured. For the elements Sr, Pb, Rb, and Th, the Peres dataset has higher concentrations compared to the Schleenhain and Profen samples. Both drill core datasets of Schleenhain and the Profen dataset have a similar elemental concentration for the considered elements.

The Schleenhain-lithology datasets are sampled at specific geological layers, which enables us to test the element distribution for the following lithologies: coal, gravel, sand, loam, clay and mixtures (see Figure 7). The highest element concentrations are in the clay and coal lithologies. The elements Pb, Ti, Rb, and Th are particularly high for clay samples. Zn concentrations are high for a few coal samples, and Sr and Y have high concentrations for both coal and clay samples. There is quite a large distribution within these lithologies so not all coal or clay samples have a similar concentration of particular elements.

There were geochemical differences between the different datasets (see Figure 6), there are also differences in correlation between elements for the different datasets (Figure 8). For example, between Sr and Rb, the Schleenhain-waste and Profen datasets have a high correlation (>0.8) while the Schleenhain-lithology only has a correlation coefficient of 0.39. The samples that do not fit in the general trend between these elements are a few coal samples from the Schleenhain-lithology dataset. Pb and Th are the only elements that have a high correlation among all the datasets.
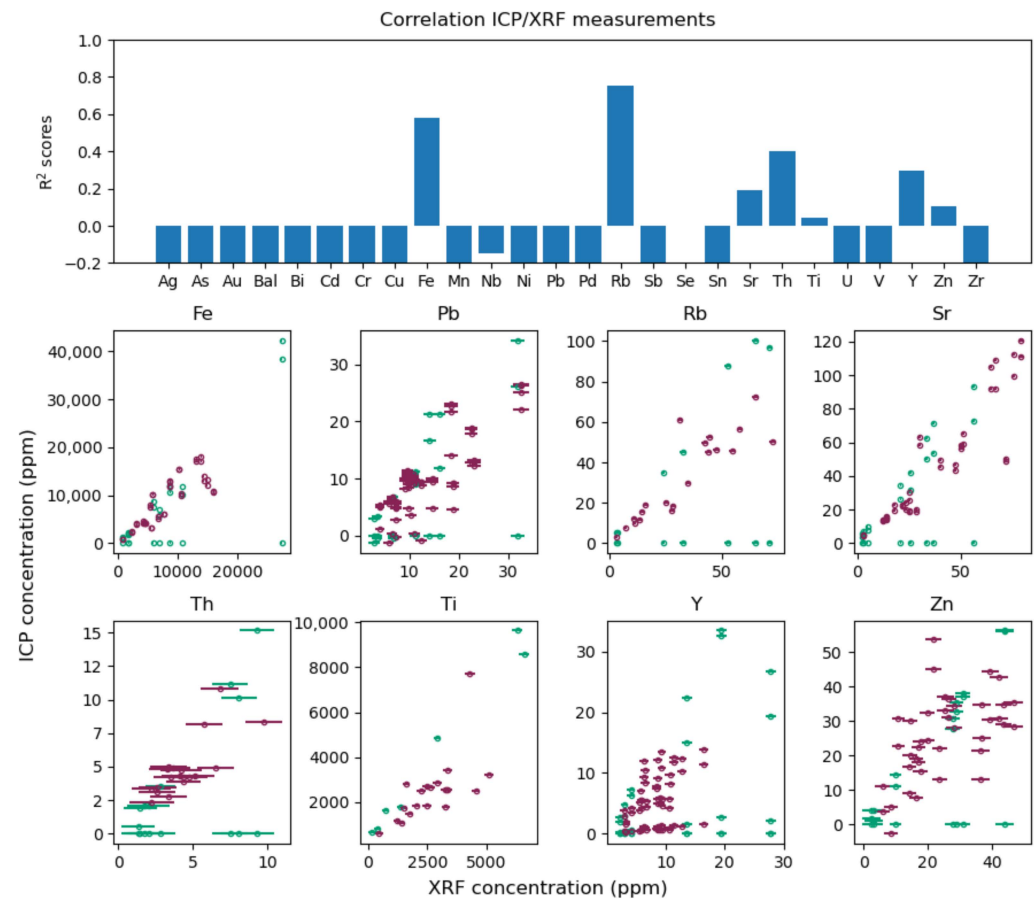
**Figure 5.** $R^2$ values indicating correlation between XRF and ICP-MS data for the Schleenhain-waste (red) and Profen (green) datasets. For elements with a positive $R^2$, the scatter plots show the measurement results of both sensors with error bars indicating the 1.5 sigma standard deviation of the XRF.
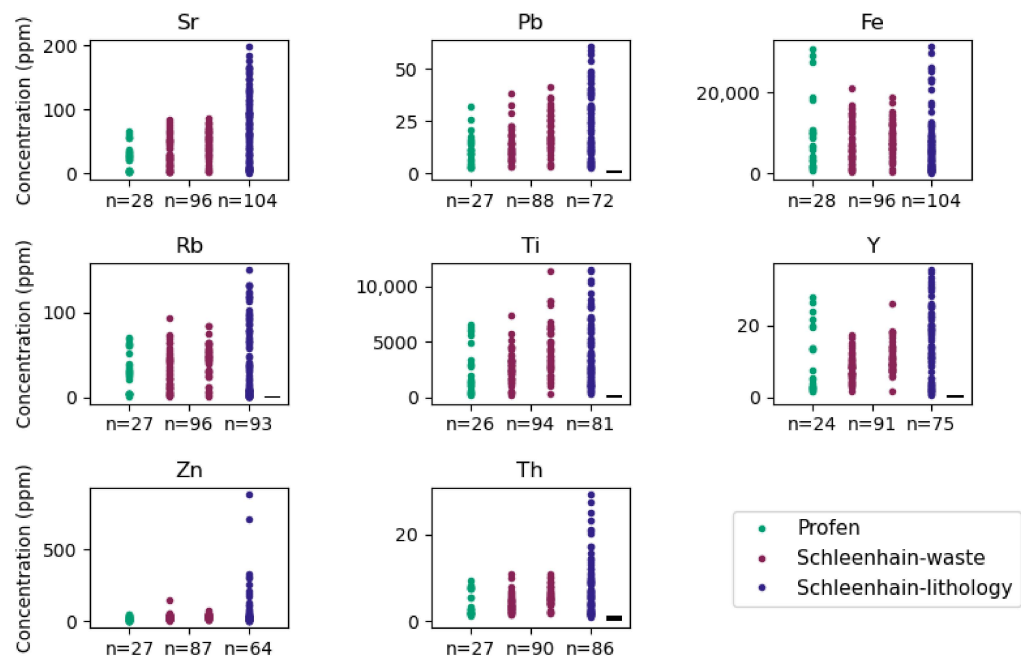


**Figure 6.** Measured metal content in mine waste for both the Profen and Schleenhain mines. The n-number indicates the number of samples with values above the XRF detection limit.
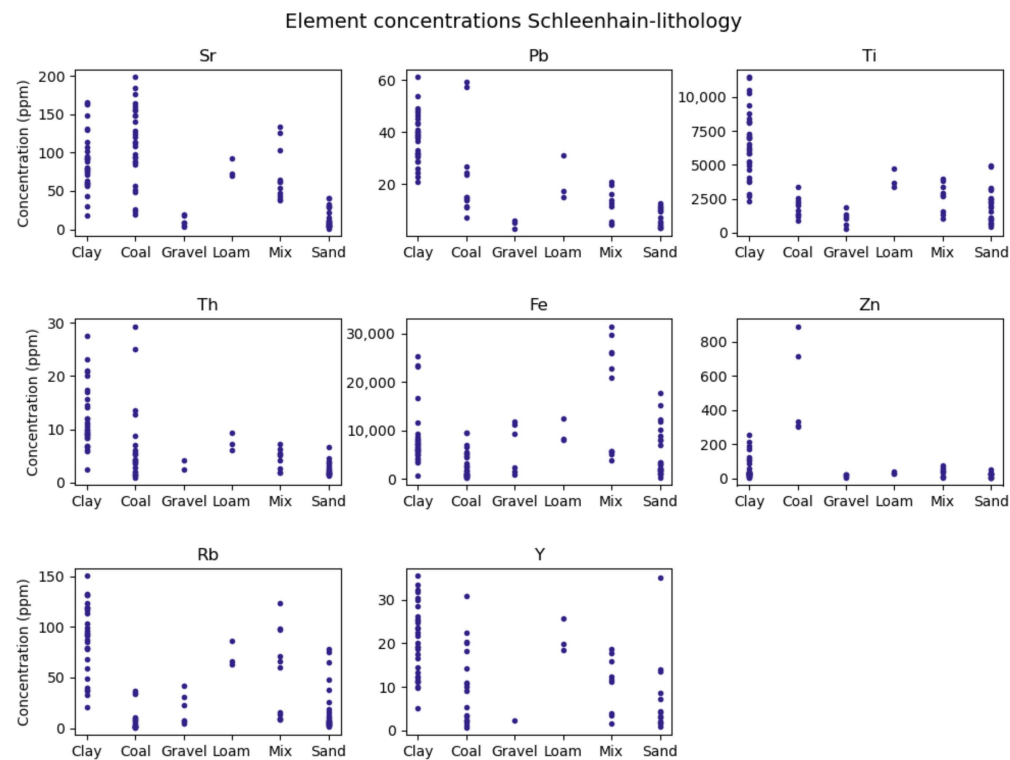
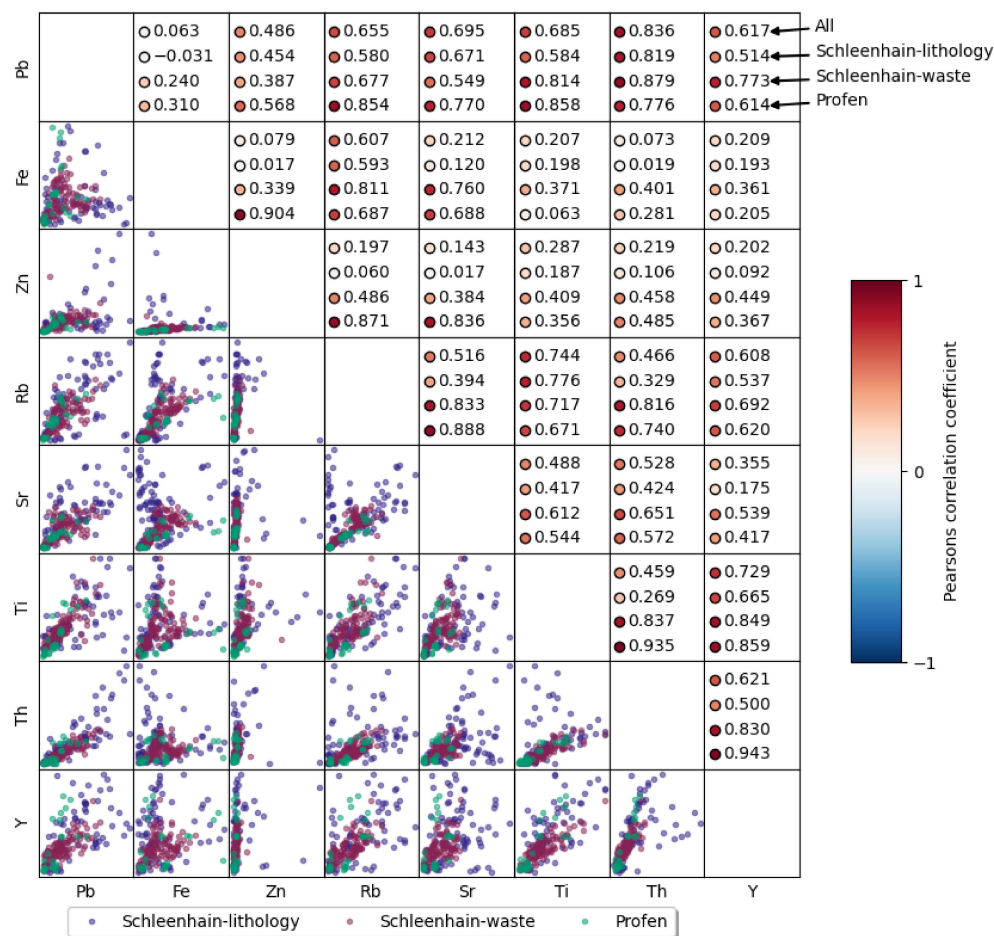**Figure 7.** Element concentration grouped by lithology of the Schleenhain-lithology dataset.



**Figure 8.** Correlation matrix based on the available XRF data from the different datasets.

### 4.2. Spectral Analysis

The spectral datasets consist of reflectance data measured in different wavelength ranges. The visible and shortwave–infrared wavelength ranges were only measured for the Schleenhain-lithology dataset and the midwave and longwave for all datasets. Therefore, the compositional differences between datasets are based on the FTIR data (Section 4.2.1) and the spectral differences between wavelength ranges are only based on the Schleenhain-lithology dataset (Section 4.2.2). PCA has been used to reduce the dimensions of the data and indicate the most variance within the datasets (Figures 9 and 10). Specific samples that seem unique or characteristic based on the PCA and visual comparison are highlighted in the plots and their spectra are presented in Figure 11. With grey boxes and dashed lines, specific spectral features are highlighted.
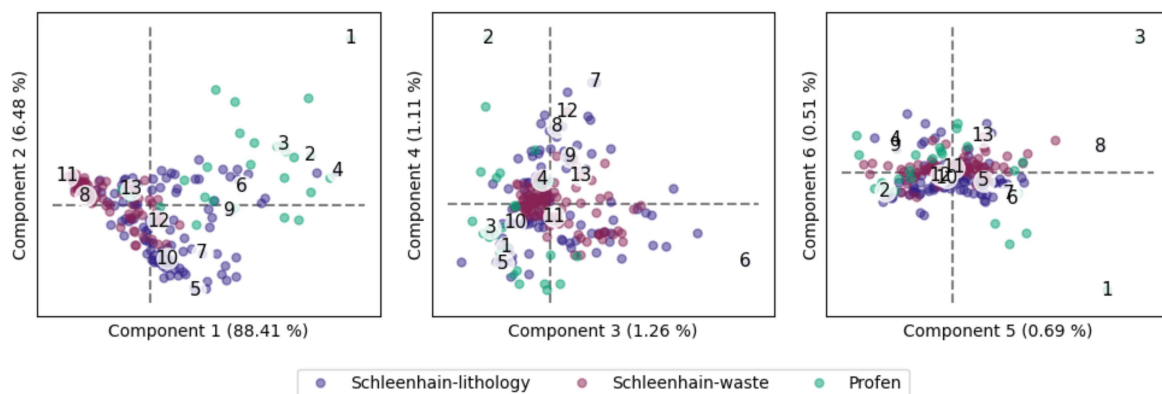


**Figure 9.** PCA score plots for all datasets. The numbers indicate the score values of specific samples plotted in the spectral plot in Figure 11.
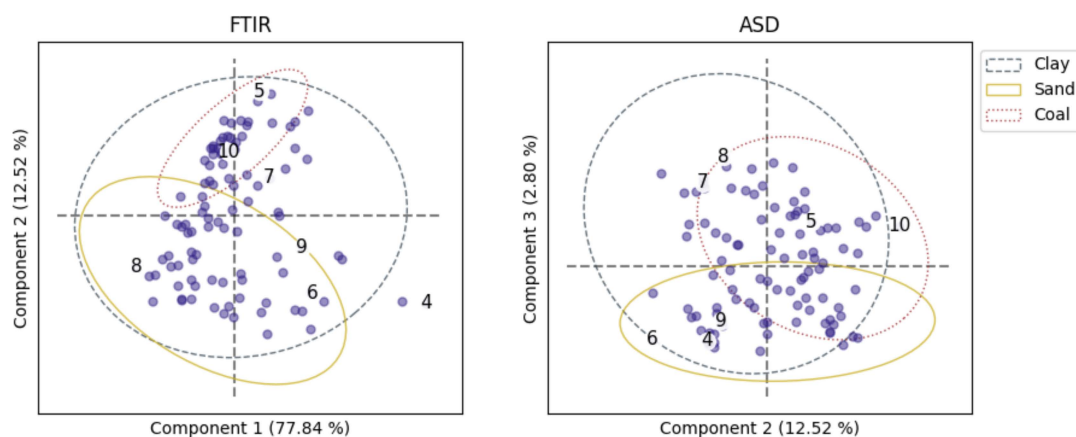


**Figure 10.** PCA score plots for the Schleenhain-lithology. Left: FTIR, right: ASD. The numbers indicate the score values of specific samples plotted in the spectral plot in Figure 11.

#### 4.2.1. Spectral Difference Datasets

The PCA score plots show that most of the variance (component 1) is between the samples from the three datasets. The first component explains over 88% of the variance and shows the highest score values for the Profen samples and the lowest values for the samples from the Schleenhain-waste. The Schleenhain-lithology plots are in between with some overlap between both of the datasets. Some individual samples have extremer score values for the other components.
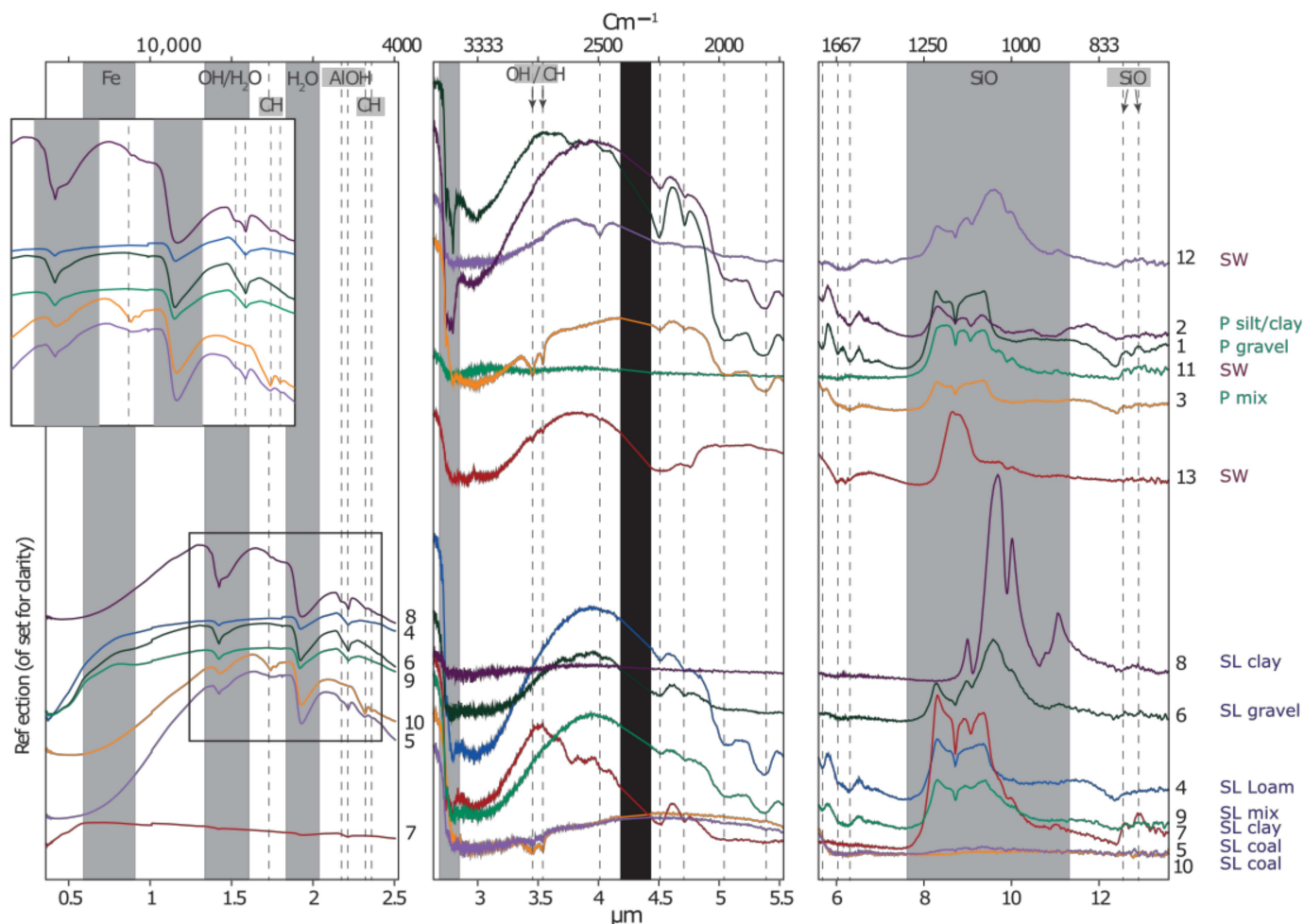
**Figure 11.** Specific spectra from the three datasets. Numbers correspond with numbers in the PCA plots in Figures 9 and 10. These numbers are not the sample numbers used in the datasets, colors of lines are used for clarity and do not contain any additional information. The *x*-axis on the bottom presents the wavelength, and the x-axis on the top presents the wavenumber.

### 4.2.2. Spectral Differences Wavelength Ranges

When the PCA score plots of both the FTIR and ASD data are compared, it can be noticed that especially the lithologies coal, clay and sand can best be distinguished in the FTIR dataset. In the PCA score plots based on FTIR data, component 2 separates the coal and sand samples. The clay overlaps with both lithologies. The PCA using the ASD data shows much more overlap between the lithologies. Some separation between sand and coal is visible for component 3 but it is not as distinct as with the FTIR. In all components, the clay samples overlap with both the sand and coal lithologies.

### 4.2.3. Mineralogical Interpretation

Based on the spectral features of the ASD and FTIR datasets, they are interpreted to be related to quartz, kaolinite, montmorillonite, gypsum, quartz and organics from the coal. The minerals are also confirmed by the XRD validation dataset, and only illite and pyrite are found with XRD but are not recognized in the spectral datasets. Pyrite is a metal sulfide, which is spectrally featureless in the measured wavelength range and so would be difficult to identify [39]. The lack of spectral features for some of the coals could indicate the presence of pyrite but more data are required to confirm this. Illite has characteristic absorption features near 2.35 and 2.44 μm which are not recognized in neither of the spectra. In the longer wavelengths, illite and montmorillonite are hard to distinguish, especially because it seems that in our samples, the samples that might be related to either

of the minerals are in combination with very dominant quartz features. Kaolinite, however, has clear spectral features such as the double feature near 2.16 and 2.21 μm and the clear spectral peaks near 9.5, 9.9 and 11 μm, which makes it easy to recognize spectrally. Based on the spectra, it seems to be low crystalline kaolinite since the feature near 2.165 μm is shallow compared to the 2.21 μm feature [40].

The coal samples are besides a double feature near 3.5 μm featureless in the longer wavelength ranges. In the ASD data, it contains a broad spectral feature near 1.7 μm and a double feature near 2.3 and 2.35 μm. Studies such as the one authored by Langa et al. [33] show that coals with higher organic content have flatter spectra.

*4.3. Geochemical Modelling*

Proceeding the geochemical exploration, we will focus on the infrared and geochemical data integration by developing various models, using different wavelength ranges. As described in the Methodology section, we used support vector machine regression in combination with different pre-processing techniques and hyperparameter tuning to find the optimal models. The many repetitions in the models yielded many results and are therefore presented in Appendix A, and only the $R^2$ scores of the testing dataset, for the best model for each element, are presented in Figure 12. The plots in Appendix A, show the R2 for the testing dataset (blank bars) and the average and standard deviations of the cross-validation repetitions presented in colored bars with corresponding error bars. For some elements, such as Sr, the choice of best model was obvious. The best model has the highest score values for both the training and testing dataset, with small error bars. However, for elements such as Fe, the differences between the models are smaller, scores of training and testing data are not always related, and the cross-validation scores have large standard deviations. These aspects are discussed in Discussion Section 5.3 regarding the model performance. The scatterplots corresponding to the models indicated in the bar diagram of Figure 12 are presented in Figure 13 with the original concentration on the *x*-axis and the predicted concentration on the *y*-axis. Since most of the SVR models are non-linear, except for the model of Ti, the model cannot be presented with regression coefficients as a mathematical function.
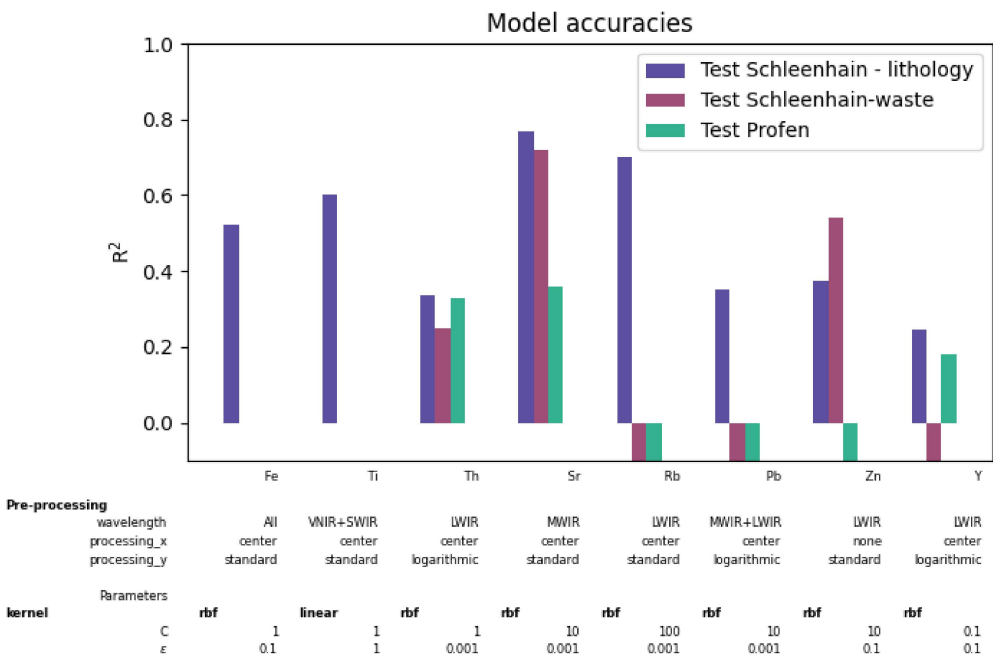


**Figure 12.** Model accuracies and parameters for each element trained on Schleenhain-lithology and tested on Schleenhain-waste and Profen datasets.
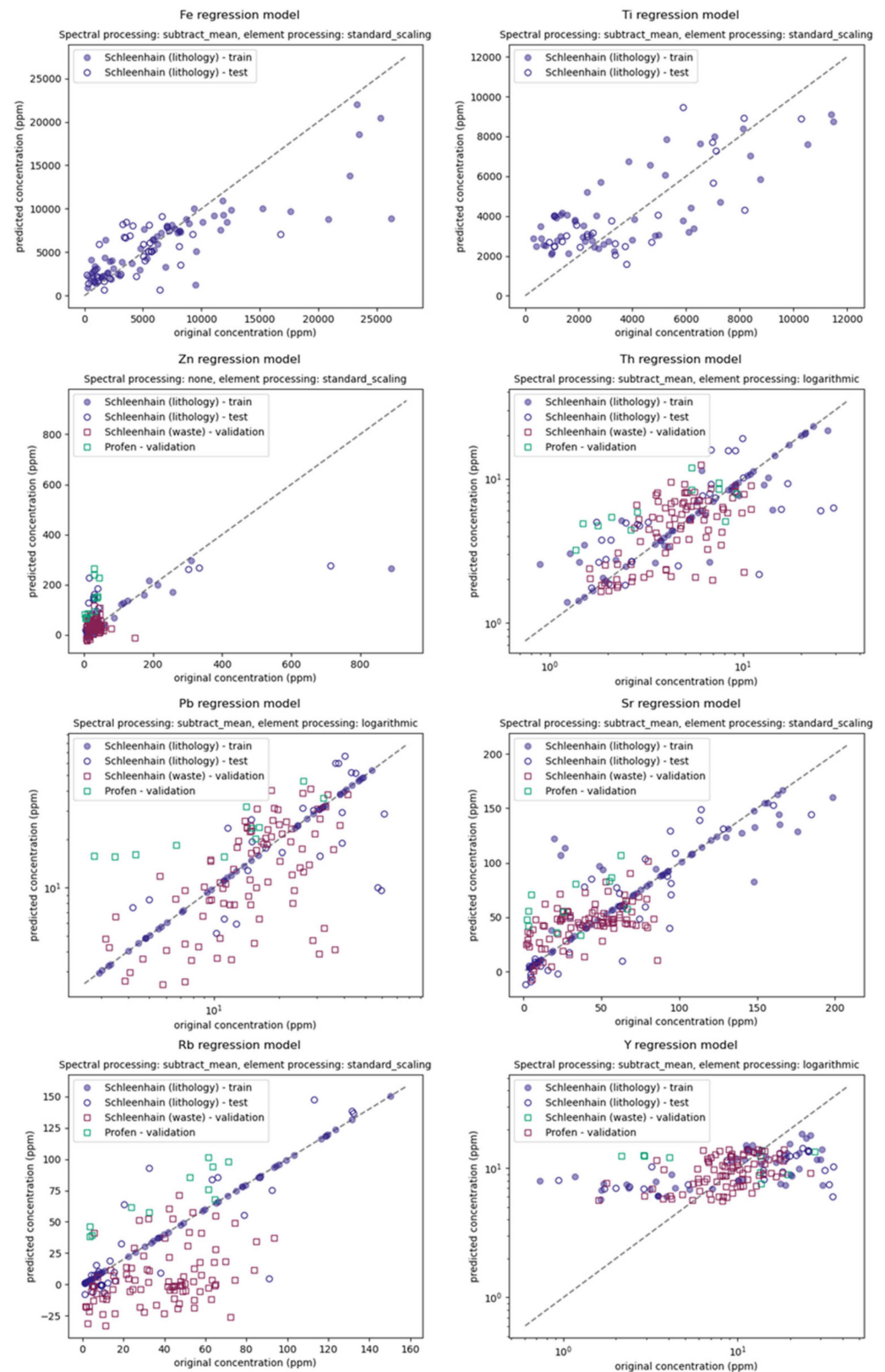
**Figure 13.** Scatter plots indicating the actual (*x*-axis) vs. predicted (*y*-axis) values.

Regarding the model parameters, it can be seen that for most elements the FTIR data are best to predict the element concentration. Only Ti performs best when only using the ASD data, and for Fe, the full wavelength range shows the best results.

Most models are based on radial basis function (rbf) kernels, and only for Ti was the linear model the best model. For the pre-processing, all models except the one for Zn performed best when the spectral data were centered, i.e., mean subtracted. For the pre-processing of the element concentration, most models performed best when the data were standard-scaled (i.e., subtract the mean and divide by the standard deviation), and only the models for Pb, Y and Th showed higher accuracies when the concentration had a logarithmic scale.

## 5. Discussion

### 5.1. Compositional Analysis

#### 5.1.1. Geochemistry

As described in the results, only for eight elements were the pXRF element concentrations considered representative for the actual rock chemistry based on the geochemical validation data from the ICP-MS (Figure 5). The geochemical analysis reveals compositional differences between the Schleenhain-lithology and the two waste sites, with higher content for the elements, Pb, Sr, Rb, Zn, and Th in the Schleenhain-lithology. These geochemical compositional differences are also evident in the correlation matrix (Figure 8) where certain element ratios, such as Th/Ti and Sr/Rb, show high correlation within the waste samples but no correlation for the lithology dataset. Also, we did not observe geochemical differences between the two mine waste drill cores, indicating similar geochemical differences between the 'fresh' and older mine waste.

The elemental composition compared for each lithology (Figure 7) shows that these five elements, with the highest content in Schleenhain-lithology, have the highest concentrations for the coal and clay lithologies. Given that coal is the product mined for, its presence in the waste is minor. Therefore, the low coal content in the waste could account for reduced element concentrations in the waste. Different from coal, clay is not of economic interest for this mine and is therefore expected in both the lithology and waste datasets. Because some elements such as Sr, Rb, and Th have higher concentrations for the Schleenhain-lithology clay samples compared to waste samples, compositional differences between clay samples in the different datasets is expected. Spectral interpretations, which will be discussed in the next section (Section 5.1.2—Mineralogy), can provide further clarification on these compositional differences.

According to Malvadkar et al. [12], the presence of inorganics in coal can be explained by multiple processes. The inorganics might have naturally existed before coal formation, or incorporated through cation exchange, or introduced by filtration. Additionally, minerals associated with coal, such as sulfides, which contain metals in their structure, could also be responsible for the high element content. The elevated metal concentrations for clays can be explained by either adsorption or ion exchange [41,42].

#### 5.1.2. Mineralogy

Although the mineralogy itself poses no direct environment concern, its presence can influence conditions such as soil stability, metal mobility, and potential acid mine drainage. Therefore, understanding the mineralogical composition is crucial for assessing possible environmental impacts guiding remediation efforts, and recognizing potential secondary resources for recovery. This section discusses the exploratory analysis and spectral information related to the mineral composition and their potential environmental impact.

The spectral differences between the three datasets can best be analyzed using the PCA based on FTIR data (Figure 9). Component 1, in particular, indicates significant spectral differences among the three datasets. Further analysis of the PCA results and visual comparison of the spectra reveal that the variance explained is due to higher spectral reflectance in the 3–5 μm wavelength range for the Profen and Schleenhain-lithology relative to the Schleenhain-waste spectra (see for example differences in spectra 1 and 11 in Figure 11). This spectral difference could be attributed to sample moisture or grain size [43], but also other aspects such as matrix effect and instrumental factors cannot be excluded.

The PCA of the Schleenhain-lithology dataset only reveals that, for both the FTIR and ASD data, most spectral variance is observed between the lithologies coal and sand, which both overlap with the clay samples. This suggest that spectral features associated with clay minerals can be observed in the coal and sand samples.

The geochemical analysis revealed compositional differences within the clay samples from Schleenhain-lithology. To determine whether these compositional differences are also reflected in mineralogy, the spectra were analyzed in detail for clay identification. Based on the ASD data, the minerals kaolinite and montmorillonite were identified, and this was further validated using the XRD data. Although XRD analysis indicated the presence of illite in some of the samples, its diagnostic features were not interpreted in the spectra. Kaolinite typically exhibits a double feature near 2.16 and 2.21 μm, with the dominance of the 2.16 μm feature depends on the mineral's crystallinity. In the analyzed samples, however, the 2.16 μm is not very dominant (see spectra 5 and 8 in Figure 11), indicating a poor crystalline kaolinite. Spectra such as 4, 6 and 9 in Figure 11, show a broad 2.2 μm feature characteristic of either illite or montmorillonite. As the spectra lack the two diagnostic features of illite near 2.347 and 2.44 μm, a broad spectral feature near 2.2 μm is most likely montmorillonite. Comparing the FTIR spectra of these samples shows that spectrum 6 also contains silica features similar to kaolinite, spectrum 4 has mainly quartz features and spectrum 9 had additional features other than quartz which could be attributed to montmorillonite.

While the geochemical analysis indicated compositional differences between coal samples, the spectra in the MWIR and LWIR regions do not exhibit spectral features except a double feature near 3.5 μm due to CH2 bonds. This spectral feature overlaps with the OH double feature common to some hydrated minerals [25], complicating the identification of coal in a mixed spectrum of coal and clay. In the SWIR range, the coal can be identified based on the 1.7 μm and double feature near 2.4 μm. More spectral features due to aromatic and aliphatic functional groups were expected in the MWIR and LWIR wavelength ranges [30]. Low grade coals, such as our lignite samples, are known to have shallower absorption features [30]; however, the study of Cepus et al. [31] on lignite samples did characterize more spectral features which could be linked to the H/C ratio of coal. However, that study used transmission spectroscopy focused on coal samples specifically including sophisticated sample preparation.

## 5.2. Infrared Spectroscopy as a Geochemical Indicator

For a comprehensive coal mine waste characterization, the geochemical and infrared spectral data were integrated. This integration uses infrared spectra for semi-quantitative analysis of element concentrations through machine learning methods. The results demonstrate that the model accuracies vary significantly depending on the modelled element, with higher accuracies ($R^2$ for the testing data), 0.77 and 0.70, for Sr and Rb, respectively. Conversely, elements like Zn, Th, Y and Pb have the lowest accuracies with an R2 below 0.4.

This approach is advantageous for simultaneous analysis of chemistry and mineralogy and offers new insights into the integration of portable sensor technologies for future mine waste analysis. It is important to note that correlation does not imply causation in the context of the interpretation of the modelling results. Therefore, the ability to model a specific element using a particular wavelength or spectral feature does not necessarily mean that the element is hosted in the mineral associated with that feature or range. Instead, it may indicate that the element and mineral are formed or deposited under similar geological conditions.

The models for Sr and Rb perform best in the longer wavelength ranges, specifically the MWIR and LWIR, while showing very low performance, particularly for Sr, in the VNIR and SWIR ranges. This indicates that the longer wavelengths are more effective for quantifying the geochemical variation. Analysis of the spectra of samples with high Sr and Rb content reveals that both elements show elevated concentrations in samples that were identified as montmorillonite. Sr and Rb are both not expected in the mineral structure

itself, as noted by [44]. This suggests that these elements are secondary and adsorbed by montmorillonite.

Although the models for Ti and Fe are not among the best in terms of accuracy, they are of particular interest because they perform best when the ASD wavelength range is included. Specifically for Ti, the models using the SWIR and ASD wavelength ranges outperform those using other wavelength ranges (see Appendix B). For Fe, only the VNIR range explains some of the geochemical variance, as the SWIR has low $R^2$ values, indicating that it does not explain any of the geochemical variance.

Examining the spectral features in these ranges for samples with high and low Ti content reveals a slight trend related to the dominance of the 2.156 μm feature of kaolinite. The depth of this feature compared to kaolinite feature near 2.21 μm serves as a proxy for its crystallinity [40]. Based on these analyses, it is hypothesized that Ti is substituted for Al in kaolinite, reducing its crystallinity [45].

With $R^2$ values lower than 0.4 and high standard errors for the calibration data, the models for Th, Pb, Y and Zn underperform compared to the models for the other elements. It is possible that the element concentration is not related to any mineralogy or that the specific mineral could not be measured with the infrared technology. Such a mineral could be sulfide which has little features in the wavelength range considered in this study but is an important mineral due to its metal sulfide bond.

### 5.3. Integration of Wide Wavelength Range Infrared Data

The different exploratory and modelling analysis demonstrate the benefit of combining both the ASD and FTIR sensors for mine waste characterization. The PCA results based on FTIR and ASD wavelength ranges show that both wavelength ranges were able to distinguish the coal, clay and sand lithologies of the Schleenhain-lithology dataset. However, there is more overlap between especially the coal and sand lithologies in the PCA plots using the ASD data compared to those generated using only the FTIR data.

The combined wavelength range has proven especially useful for the mineral interpretations. For example, spectrum 5 in Figure 11 is relatively featureless in the FTIR wavelength range but shows identifiable kaolinite features in the SWIR range. This suggests that the ASD sensor is better suited to identify minor clay content in the samples. Conversely, quartz (spectrum 7 in Figure 11) appears featureless in the ASD range but exhibits prominent features in the FTIR range, specifically the silica features between 8 and 11 μm. This observation aligns with the fact that SWIR technology is effective for identifying hydrated weathering or alteration minerals, while FTIR is more suited for identifying rock-forming minerals, such as silicates [25].

The model performances vary significantly across the different wavelength ranges considered. Often, the best geochemical model is achieved using a specific wavelength range, indicating that no single wavelength range is universally optimal for geochemical modelling. Instead, the most effective wavelength range depends on the specific element being analyzed.

### 5.4. Opportunities, Limitations and Recommendations

In this study, a methodological framework was developed to assess the use of sensor technologies for characterization of lignite mine waste. This research explored the opportunities and limitations associated with sampling strategies, sensor technologies and data analysis methods for comprehensive mineralogical and geochemical lignite mine waste characterization.

The exploratory and modelling results indicate the most effective wavelength ranges for spectral analysis and geochemical modelling. These results can inform future mine waste sorting or monitoring efforts and be scaled up to other infrared sensor platforms, such as those on conveyor belts or remote sensing systems. Integrating geochemical and infrared sensor technologies has provided valuable insights into the relationship between element concentrations and mineralogy.

For elements such as Sr (and to lesser extent, Rb), the model performances were sufficient to conclude that long-wavelength infrared data could be suitable for at least preliminary material sorting. The low regression model performances for elements Th, Zn, and Pb indicate that infrared technology is not capable of capturing their geochemical variance effectively. Therefore, for these elements, geochemical sensor technologies remain the primary sensor for geochemical assessment.

Achieving these results presents several challenges in this study, particularly regarding sampling and data acquisition processes. Sampling and measurements were conducted under various conditions, including in the field, laboratory settings, either directly on fresh drill cores or on preprocessed samples. The difference in sampling and data collection approaches could introduce limitations for mine waste characterization when using FTIR, ASD and pXRF sensor technologies. Furthermore, the varying point size of different sensors poses difficulties, especially given the heterogenous nature of mine waste samples. Without additional sample preparation, such as homogenization, obtaining corresponding measurements with different sensors has proven to be complex.

The comparison of XRF and ICP-MS measurements underscores the significance of validation data when conducting geochemical analysis with portable XRF instruments. In this study, portable XRF was employed under conditions similar to how it would be used in the field, so with minimal sample preparation. The paper of Lemiere [34] evaluates the potential and limitations of portable XRF technology, emphasizing the impact of factors such as sample heterogeneity, granularity, porosity or moisture on the measurement accuracy.

Based on our findings, it remains unclear to what extent the measuring conditions contributed to the low measurement accuracy for some of the elements. Consequently, it is uncertain whether additional sample preparations would enhance the measurement accuracy. Some elements exhibit low correlation with the ICP-MS data due to concentrations nearing the sensor's detection limits (e.g., arsenic), or high standard errors in measurements (e.g., chromium). These factors must also be considered when evaluating the geochemical models. The model performance will decrease when the input data does not represent the actual sample geochemistry. Therefore, only seven of the elements measured by the XRF are included in the data analysis of this paper.

The infrared data has inherent limitations, as not all minerals exhibit spectral features within the used wavelength range. Despite integrating both ASD and FTIR in our approach to cover an extensive range, certain minerals such as sulfides remain largely featureless in this spectral range. Therefore, lower model accuracy may result because the mineralogy associated with the element content is not captured by either of the infrared sensors. Additionally, overlapping spectral features present another challenge. Section 5.1.2 addresses some examples of challenges in mineral interpretations, including cases where spectral features may be entirely obscured by others.

For future work, it is advisable to expand the dataset to encompass the mineralogical and geochemical variation in the area. This approach would facilitate the development of a more comprehensive and robust predictive model. Additionally, it is crucial to consider sample preparation as a key aspect of future work. Proper sample preparation can help mitigate the effects of external influences such as sample inhomogeneity, soil moisture, and differences in grain size, thus improving the accuracy and reliability of the analyses.

## 6. Conclusions

- This paper presents a methodological approach for data integration of a wide wavelength range of an infrared spectral dataset and pXRF geochemical data for a comprehensive characterization of coal mine waste, using ASD, FTIR and pXRF data. These datasets were analyzed using exploratory data-analysis strategies and the geochemistry is quantitatively modelled using support vector machine regression.
- For both the mineralogical and geochemical analysis, the most variance between the samples was found between the coal, clay and sand samples.
- Geochemically there was large compositional variance between the coal and clay samples.

- The spectra did confirm compositional differences for clay, related to kaolinite and montmorillonite; however, there were little spectral differences between the coals.
- The additional value of using a broad wavelength range of infrared spectroscopy is most clear in the geochemical modelling results. Especially for the model of Sr since there are significant differences in model performances between the models trained on the different wavelength ranges.
- The wavelength ranges measured with the FTIR seems best to capture the presence of certain minerals. The ASD data are able to capture minor clay and coal contents and small spectral differences of clay minerals that can be linked to, for example, the crystallinity of the mineral.
- The results show the importance of representative sampling, due to the heterogeneous nature of mine waste material and the different point size of the sensors.
- Based on our exploratory and data integration analysis, it can be concluded that there is no single method nor sensor that fully captures all compositional variance, and thereby this emphasizes the need for sensor integration for comprehensive characterization of the waste.
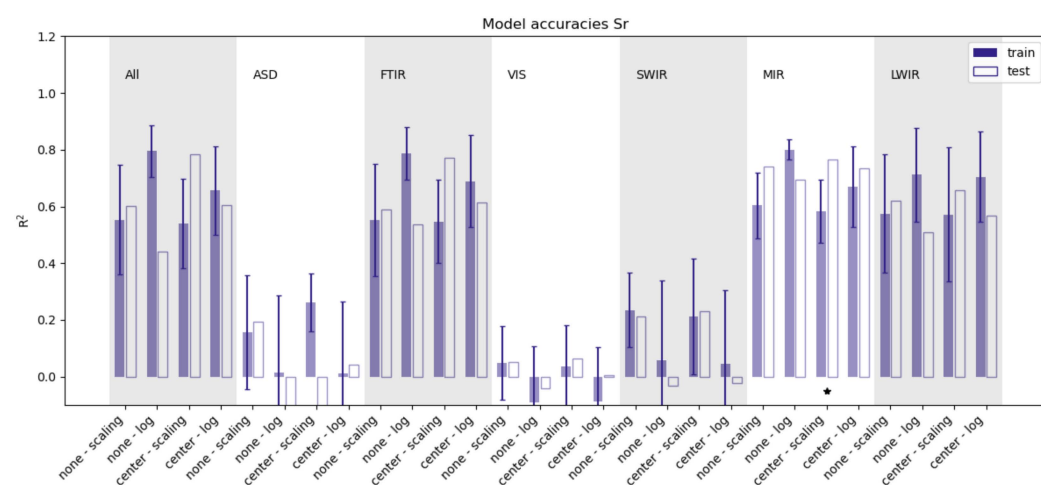
## Appendix A



**Figure A1.** Modeling results for strontium (Sr) across all repetitions, showing the impact on model accuracies of various wavelength and pre-processing steps.
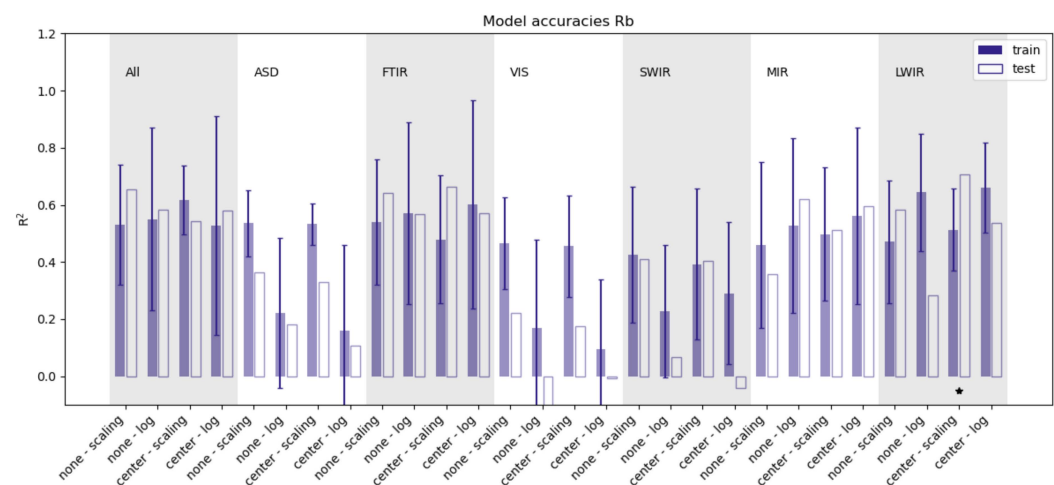
**Figure A2.** Modeling results for rubidium (Rb) across all repetitions, showing the impact on model accuracies of various wavelength and pre-processing steps.
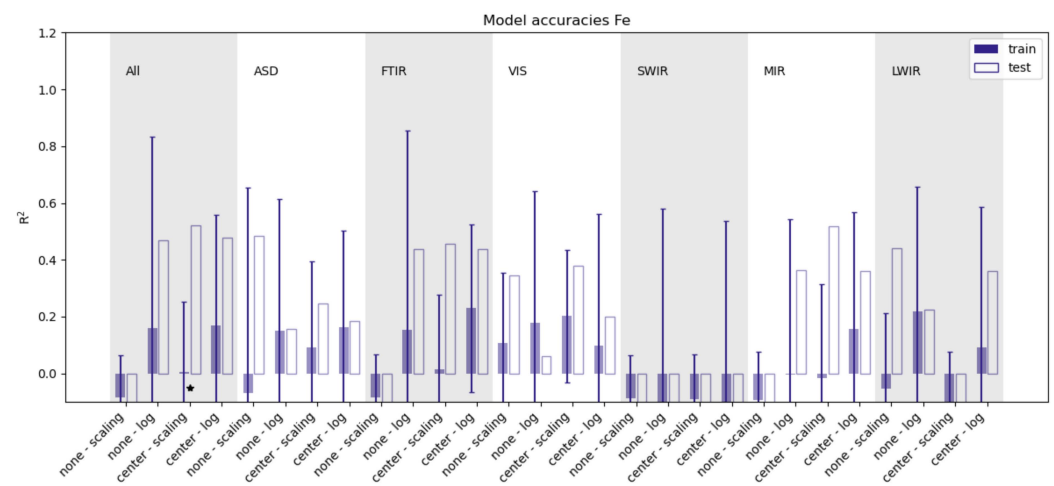


**Figure A3.** Modeling results for iron (Fe) across all repetitions, showing the impact on model accuracies of various wavelength and pre-processing steps.
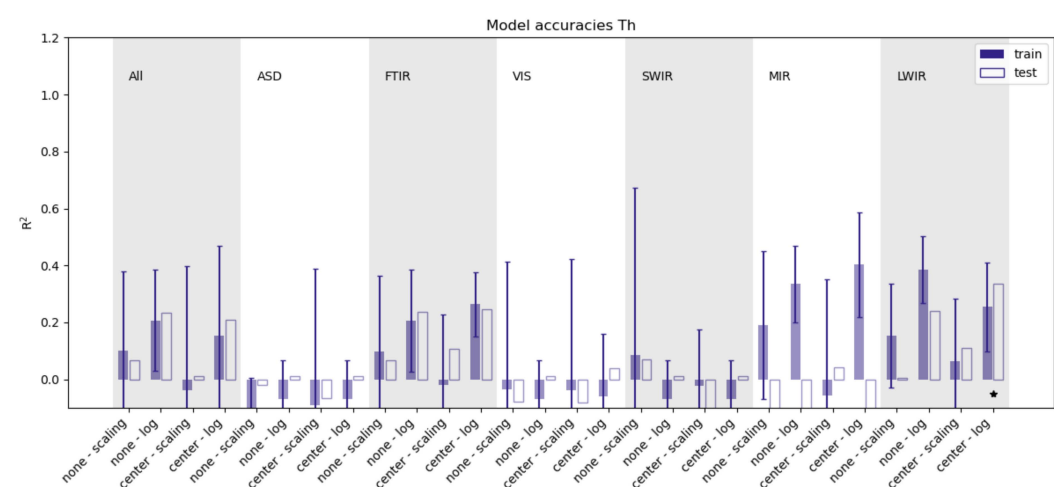


**Figure A4.** Modeling results for thorium (Th) across all repetitions, showing the impact on model accuracies of various wavelength and pre-processing steps.
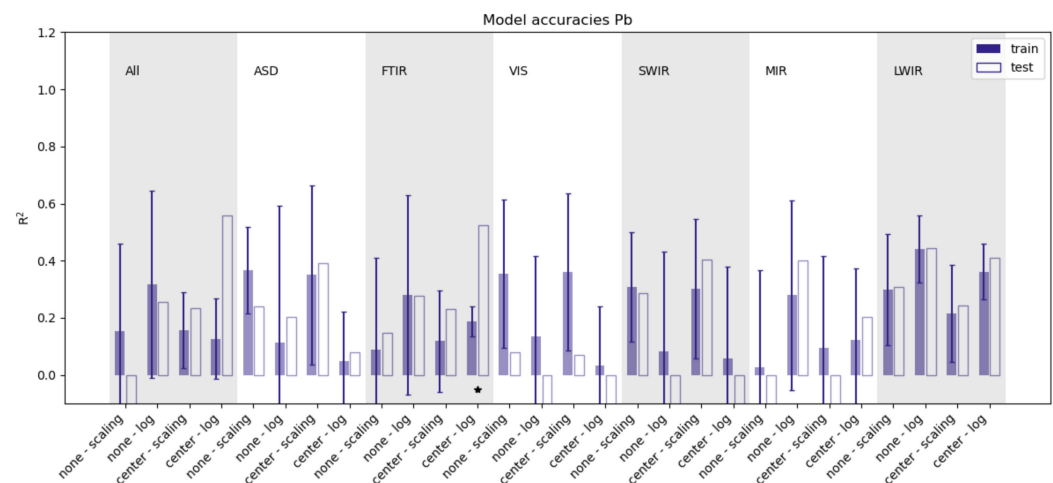
**Figure A5.** Modeling results for lead (Pb) across all repetitions, showing the impact on model accuracies of various wavelength and pre-processing steps.
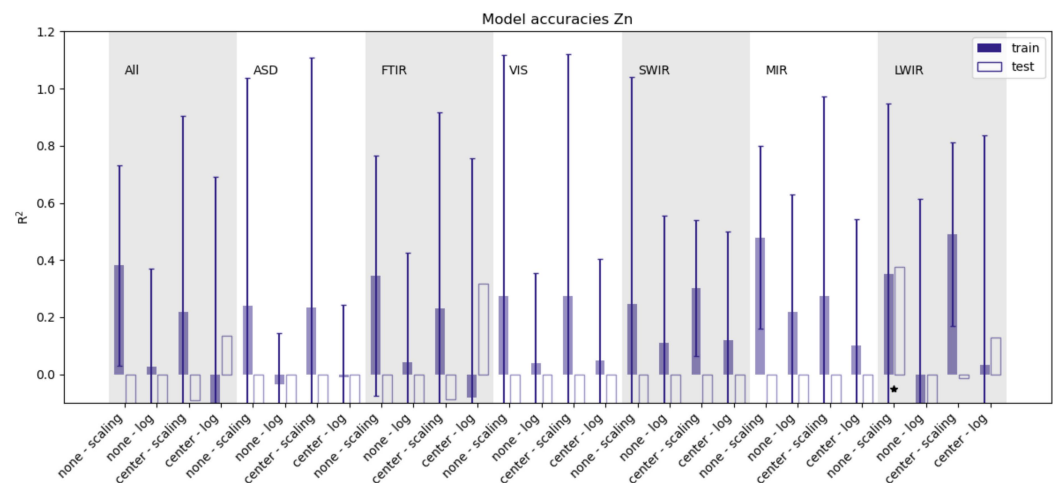


**Figure A6.** Modeling results for zinc (Zn) across all repetitions, showing the impact on model accuracies of various wavelength and pre-processing steps.
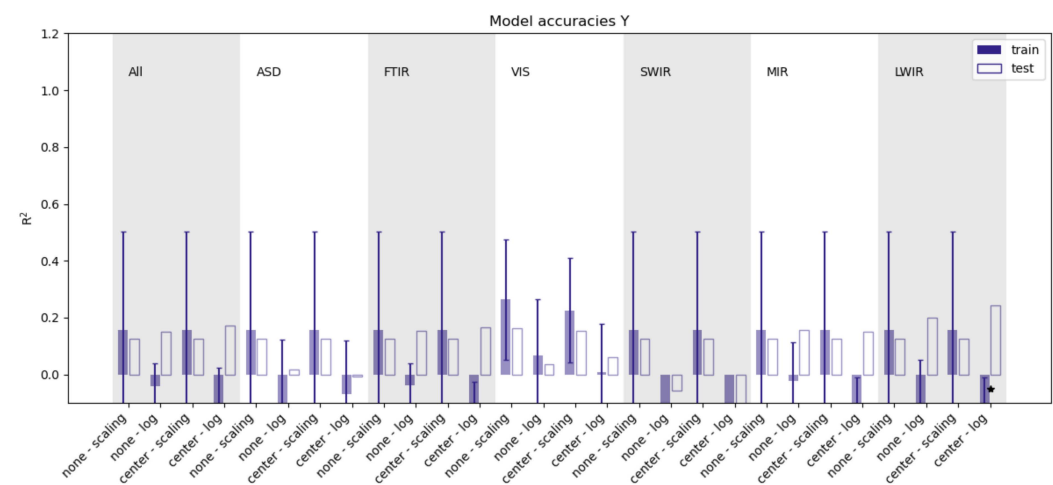


**Figure A7.** Modeling results for yttrium (Y) across all repetitions, showing the impact on model accuracies of various wavelength and pre-processing steps.
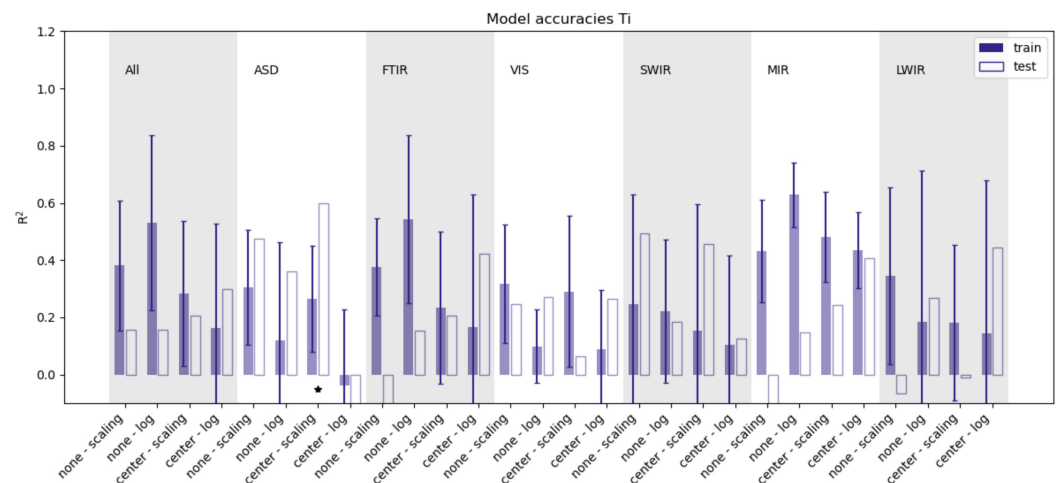
**Figure A8.** Modeling results for titanium (Ti) across all repetitions, showing the impact on model accuracies of various wavelength and pre-processing steps.

## Appendix B

**Table A1.** XRD results from the Schleenhain-waste dataset.

| Sample | Mineral 1 | Mineral 2 | Mineral 3 | Mineral 4 | Mineral 5 | Mineral 6 |
|--------|-----------|-----------|-----------|-----------|-----------|-----------|
| 1-01-2 | Quartz | Kaolinite | | | | |
| 1-03-1 | Quartz | Illite | Kaolinite | | | |
| 1-06-1 | Quartz | Illite | | | | |
| 1-07-1 | Quartz | | | | | |
| 1-08-1 | Montmorillonite | Illite | Kaolinite | Pyrite | Arsenopyrite | Titanite |
| 1-10-1 | Montmorillonite | Illite | Kaolinite | Pyrite | | |
| 1-11-1 | Illite | Montmorillonite | Kaolinite | | | |
| 1-12-1 | Quartz | Illite | Montmorillonite | Kaolinite | | |
| 1-14-1 | Quartz | Illite | Kaolinite | | | |
| 1-16-1 | Illite | Kaolinite | | | | |
| 1-19-1 | Illite | Quartz | Kaolinite | | | |
| 1-20-1 | Quartz | Illite | Kaolinite | | | |
| 1-22-1 | Quartz | Illite | Kaolinite | | | |
| 1-23-1 | Illite | Kaolinite | | | | |
| 1-26-1 | Quartz | Illite | Kaolinite | | | |
| 1-27-1 | Quartz | Kaolinite | | | | |
| 1-30-1 | Quartz | Kaolinite | | | | |
| 1-34-1 | Quartz | | | | | |

## References

1. Benndorf, J.; Restrepo, D.A.; Merkel, N.; John, A.; Buxton, M.; Guatame-Garcia, A.; Dalm, M.; de Waard, B.; Flores, H.; Möllerherm, S. TRIM4Post-Mining: Transition information modelling for attractive post-mining landscapes—A conceptual framework. *Mining* **2022**, *2*, 248–277. [CrossRef]
2. Gerwin, W.; Raab, T.; Birkhofer, K.; Hinz, C.; Letmathe, P.; Leuchner, M.; Roß-Nickoll, M.; Rüde, T.; Trachte, K.; Wätzold, F. Perspectives of lignite post-mining landscapes under changing environmental conditions: What can we learn from a comparison between the Rhenish and Lusatian region in Germany? *Environ. Sci. Eur.* **2023**, *35*, 36. [CrossRef]
3. Sloss, L.; Coal Mine Site Reclamation. IEA Clean Coal Centre; 2013; p. 70. Available online: https://www.researchgate.net/profile/Lesley-Sloss/publication/337487243_Coal_mine_site_reclamation/links/5ddbb420a6fdccdb446324e4/Coal-mine-site-reclamation.pdf (accessed on 26 March 2024).
4. Maest, A.S. Remining for renewable energy metals: A review of characterization needs, resource estimates, and potential environmental effects. *Minerals* **2023**, *13*, 1454. [CrossRef]
5. Mielke, C.; Boesche, N.K.; Rogass, C.; Kaufmann, H.; Gauert, C.; De Wit, M. Spaceborne mine waste mineralogy monitoring in South Africa, applications for modern push-broom missions: Hyperion/OLI and EnMAP/Sentinel-2. *Remote Sens.* **2014**, *6*, 6790–6816. [CrossRef]

6. Ren, H.; Zhao, Y.; Xiao, W.; Hu, Z. A review of UAV monitoring in mining areas: Current status and future perspectives. *Int. J. Coal Sci. Technol.* **2019**, *6*, 320–333. [CrossRef]

7. Peukert, D.; Xu, C.; Dowd, P. A review of sensor-based sorting in mineral processing: The potential benefits of sensor fusion. *Minerals* **2022**, *12*, 1364. [CrossRef]

8. Mibrag. Tagebau Vereinigtes Schleenhain. Available online: https://www.mibrag.de/de-de/geschaeftsfelder/bergbau/tagebau-vereinigtes-schleenhain (accessed on 17 February 2023).

9. Eissmann, L. Quaternary geology of eastern Germany (Saxony, Saxon–Anhalt, south Brandenburg, Thüringia), type area of the Elsterian and Saalian stages in Europe. *Quat. Sci. Rev.* **2002**, *21*, 1275–1346. [CrossRef]

10. Eissmann, L. Tertiary geology of the Saale–Elbe region. *Quat. Sci. Rev.* **2002**, *21*, 1245–1274. [CrossRef]

11. Standke, G.; Escher, D.; Fischer, J.; Rascher, J. *Das Tertiär Nordwestsachsens–Ein Geologischer Überblick.–1–162*; Sächsisches Landesamt Für Umwelt, Landwirtschaft und Geologie: Dresden, Germany, 2010.

12. Malvadkar, S.B.; Forbes, S.; McGrul, G. Formation of coal resources. *Encycl. Energy* **2004**, *1*, 529–550. [CrossRef]

13. Blodau, C. A review of acidity generation and consumption in acidic coal mine lakes and their watersheds. *Sci. Total Environ.* **2006**, *369*, 307–332. [CrossRef]

14. Chaerun, S.K.; Jeremy, E.; Chaerun, R.I.; Fathira, R.L.; Toynbee, M.I.; Supandi, S.; Sato, T. Coal mine wastes: Effective mitigation of coal waste slurry and acid mine drainage through bioflocculation using mixotrophic bacteria as bioflocculants. *Int. J. Coal Geol.* **2023**, *279*, 104370. [CrossRef]

15. Krümmelbein, J.; Bens, O.; Raab, T.; Anne Naeth, M. A history of lignite coal mining and reclamation practices in Lusatia, eastern Germany. *Can. J. Soil Sci.* **2012**, *92*, 53–66. [CrossRef]

16. Beier, T.; Opp, C.; Hahn, J.; Zitzer, N. Sink and Source Functions for Metal(loid)s in Sediments and Soils of Two Water Reservoirs of the Ore Mountains, Saxony, Germany. *Appl. Sci.* **2022**, *12*, 6354. [CrossRef]

17. Islam, N.; Rabha, S.; Subramanyam, K.; Saikia, B.K. Geochemistry and mineralogy of coal mine overburden (waste): A study towards their environmental implications. *Chemosphere* **2021**, *274*, 129736. [CrossRef]

18. Mach, K.; Teodoridis, V.; Grygar, T.M.; Kvaček, Z.; Suhr, P.; Standke, G. An evaluation of palaeogeography and palaeoecology in the Most Basin (Czech Republic) and Saxony (Germany) from the late Oligocene to the early Miocene. *Neues Jahrb. Geol. Paläontol. Abh.* **2014**, *272*, 13–45. [CrossRef]

19. Rascher, J.; Escher, D.; Fischer, J. Zur stratigraphischen Gliederung des obereozänen Hauptflözkomplexes (Thüringer und Bornaer Hauptflöz) in der Leipziger Bucht. *Z. Dtsch. Ges. Geowiss.* **2008**, *159*, 105–116.

20. Pires, M.; Fiedler, H.; Teixeira, E.C. Geochemical distribution of trace elements in coal: Modelling and environmental aspects. *Fuel* **1997**, *76*, 1425–1437. [CrossRef]

21. Dalm, M.; Buxton, M.; Van Ruitenbeek, F. Ore–waste discrimination in epithermal deposits using near-infrared to short-wavelength infrared (NIR-SWIR) hyperspectral imagery. *Math. Geosci.* **2019**, *51*, 849–875. [CrossRef]

22. Desta, F.; Buxton, M. Image and point data fusion for enhanced discrimination of ore and waste in mining. *Minerals* **2020**, *10*, 1110. [CrossRef]

23. Körting, F.; Hernandez, J.; Koirala, P.; Lehman, M.; Monecke, T.; Lindblom, D. Development of the HySpex hyperspectral drill core scanner: Case study on exploration core from the Au-rich LaRonde-Penna volcanogenic massive sulfide deposit, Quebec, Canada. *Hyperspectral Imaging Appl. II* **2023**, *12338*, 25–37. [CrossRef]

24. Van Duijvenbode, J.; Cloete, L.; Shishvan, M.S.; Buxton, M. Material fingerprinting as a tool to investigate between and within material type variability with a focus on material hardness. *Miner. Eng.* **2022**, *189*, 107885. [CrossRef]

25. Laukamp, C.; Rodger, A.; LeGras, M.; Lampinen, H.; Lau, I.C.; Pejcic, B.; Stromberg, J.; Francis, N.; Ramanaidou, E. Mineral physicochemistry underlying feature-based extraction of mineral abundance and composition from shortwave, mid and thermal infrared reflectance spectra. *Minerals* **2021**, *11*, 347. [CrossRef]

26. Madejová, J.; Gates, W.P.; Petit, S. IR spectra of clay minerals. *Dev. Clay Sci.* **2017**, *8*, 107–149.

27. Burns, R.G. *Mineralogical Applications of Crystal Field Theory*; Cambridge University Press: Cambridge, UK, 1993.

28. Van der Meer, F. Near-infrared laboratory spectroscopy of mineral chemistry: A review. *Int. J. Appl. Earth Obs. Geoinf.* **2018**, *65*, 71–78. [CrossRef]

29. Clark, R.N.; King, T.V.; Klejwa, M.; Swayze, G.A.; Vergo, N. High spectral resolution reflectance spectroscopy of minerals. *J. Geophys. Res. Solid Earth* **1990**, *95*, 12653–12680. [CrossRef]

30. Balachandran, M. Role of infrared spectroscopy in coal analysis—An investigation. *Am. J. Anal. Chem.* **2014**, *2014*, 45156. [CrossRef]

31. Cepus, V.; Borth, M.; Seitz, M. IR spectroscopic characterization of lignite as a tool to predict the product range of catalytic decomposition. *Int. J. Clean Coal Energy* **2016**, *5*, 13. [CrossRef]

32. Clark, R.N.; Curchin, J.M.; Hoefen, T.M.; Swayze, G.A. Reflectance spectroscopy of organic compounds: 1. Alkanes. *J. Geophys. Res. Planets* **2009**, *114*, E03001. [CrossRef]

33. Langa, W.; Ndou, C.; Zieger, L.; Harris, P.; Wagner, N. Hyperspectral imaging of coal core: A focus on the visible-near-shortwave infrared (VN-SWIR) region. *Int. J. Coal Geol.* **2024**, *284*, 104456. [CrossRef]

34. Lemiere, B. A review of pXRF (field portable X-ray fluorescence) applications for applied geochemistry. *J. Geochem. Explor.* **2018**, *188*, 350–363. [CrossRef]

35. Jamieson, H.E.; Walker, S.R.; Parsons, M.B. Mineralogical characterization of mine waste. *Appl. Geochem.* **2015**, *57*, 85–105. [CrossRef]

36. Wold, S.; Esbensen, K.; Geladi, P. Principal component analysis. *Chemom. Intell. Lab. Syst.* **1987**, *2*, 37–52. [CrossRef]

37. Freedman, D.A. *Statistical Models: Theory and Practice*; Cambridge University Press: Cambridge, UK, 2009.

38. Tóth, G.; Hermann, T.; Da Silva, M.; Montanarella, L. Heavy metals in agricultural soils of the European Union with implications for food safety. *Environ. Int.* **2016**, *88*, 299–309. [CrossRef] [PubMed]

39. Hatch, J.; Gluskoter, H.; Lindahl, P. Sphalerite in coals from the Illinois Basin. *Econ. Geol.* **1976**, *71*, 613–624. [CrossRef]

40. Petit, S.; Madejova, J.; Decarreau, A.; Martin, F. Characterization of octahedral substitutions in kaolinites using near infrared spectroscopy. *Clays Clay Miner.* **1999**, *47*, 103–108. [CrossRef]

41. Uddin, M.K. A review on the adsorption of heavy metals by clay minerals, with special focus on the past decade. *Chem. Eng. J.* **2017**, *308*, 438–462. [CrossRef]

42. Ugwu, I.M.; Igbokwe, O.A. Sorption of heavy metals on clay minerals and oxides: A review. *Adv. Sorpt. Process Appl.* **2019**, *2019*, 1–23. [CrossRef]

43. Salisbury, J.W.; Wald, A. The role of volume scattering in reducing spectral contrast of reststrahlen bands in spectra of powdered minerals. *Icarus* **1992**, *96*, 121–128. [CrossRef]

44. Liu, H.-C.; Hsieh, J.-Y.; Chen, Y.-H.; You, C.-F.; Jiang, W.-T.; Wen, H.-Y. Adsorption and Desorption Behaviors of Sr on Montmorillonite: A Triple Sr Isotope Perspective. *ACS Earth Space Chem.* **2022**, *6*, 2250–2260. [CrossRef]

45. Pineau, M.; Mathian, M.; Baron, F.; Rondeau, B.; Deit, L.L.; Allard, T.; Mangold, N. Estimating kaolinite crystallinity using near-infrared spectroscopy: Implications for its geology on Earth and Mars. *Am. Mineral.* **2022**, *107*, 1453–1469. [CrossRef]